Aerospace Systems
https://doi.org/10.1007/s42401-023-00267-w

ORIGINAL PAPER

Rocket-based versus solar wing-tail Martian UAVs: design, analysis, and trade studies

Elena Karpovich[1] · Timur Kombaev[1] · Djahid Gueraiche[1] · Dmitriy Strelets[1]

Received: 11 September 2023 / Revised: 25 October 2023 / Accepted: 30 November 2023

Abstract
In this study, a rocket-based UAV and a solar wing-tail Martian UAV were designed and assessed against a set of criteria established using a house of quality chart. For the design, analysis, trade studies, and optimization, MATLAB and XFLR5 were used. The optimized versions of the two configurations feature the same wing and tail airfoils, the same wing and tail planforms, different dimensions, weight, and performance. Therefore, distinct types of scientific missions are suitable for these aircraft. The results of the study extend our understanding of the capabilities of a Martian fixed-wing airplane in terms of payload mass, hence its scientific value, as well as in terms of its planform geometry and airfoil shapes.

Keywords Mars exploration · Aircraft design · LEMFEV · Low Reynolds numbers

1 Introduction

For several decades, scientists have been exploring Mars using orbiting spacecraft and rovers. Orbiters cover large areas and provide images of the planet surface with a resolution limited to a few meters, while rovers can analyze the composition of soil and rocks. In contrast, an aircraft flying at a low altitude above the surface of Mars will carry out a whole range of specific scientific research. For example, it will map an area several orders of magnitude larger than a rover, with a resolution much higher than the resolution offered by modern satellites. In addition, it will gather atmospheric data at different altitudes.

The earliest of Martian airplane projects was Mini-Sniffer, an aircraft with a wingspan of 6.7 m, powered by a hydrazine engine [1]. Since then, significant improvements related to aerodynamic design, engine concepts, energy storage, and materials have expanded the range of options for Martian unmanned aerial vehicles. Among the proposed projects, the most famous are the ARES (Aerial Photography of the Environment on a Regional Scale) from the NASA Langley Research Center [2] and the Remotely Piloted Vehicle for Mars Exploration [3]. Other projects of Martian unmanned aerial vehicles with a wide variety of concepts have been studied, such as gliders, including those with inflatable wings [4, 5], helicopters [6], and flying insect robots [7].

The design of a Martian aircraft is driven by the local low atmospheric density, low speed of sound, low temperature, low Reynolds numbers, powerful dust storms, electrical phenomena, and carbon dioxide carving [8, 9]. For a lander, Martian rugged terrain excludes the conventional take-off and landing options. The need to deliver the aircraft to Mars and the exposure to space radiation affect the aircraft's aerodynamic layout, structural design, and weight specification. The target operating area, altitude, and season may significantly affect the design decisions in terms of aircraft configuration, geometry, and power plant type.

An aircraft intended for Mars exploration can be designed to perform single-flight or multiple-flight missions.

A single-flight aircraft will conduct in-flight measurements and, if equipped with a device to perform a single controlled soft landing, it will also serve as a scientific platform for measuring parameters of interest on the surface. A vertical take-off and landing vehicle can either perform profile measurements in the planetary boundary layer on the required timescales or carry instruments to the prescribed sites and perform on-surface measurements.

Propulsion options potentially feasible for Martian conditions include the following:

– Rocket (liquid or solid) and

✉ Elena Karpovich
karpovichea@mai.ru

[1] Aircraft Design and Certification Department, Moscow Aviation Institute, Moscow, Russia

Published online: 04 January 2024

Table 1 The baseline LEMFEV configurations

LEMFEV configuration	LEMFEV versions	Power plant	Generic mission profile
Conventional wing-tail	WT1	Solar cells + battery for overnight flight + electric motor + propeller	One extended flight (day and night); longitude is limited
	WT3	Rocket engine	One flight
	WT4	Hydrazine engine + propeller	One flight
Vertical take-off and landing (VTOL) Boxwing	BW1	Solar cells + battery for overnight flight + electric motor + propeller	Several flights
	BW3	Rocket engine	One flight
	BW4	Hydrazine engine + propellers	Several flights

– Propeller (driven by various power sources).

For the science Martian UAV developed in this study, called the Long Endurance Mars Exploration Flying Vehicle (LEMFEV), the baseline configurations and associated scientific missions are presented in Table 1.

This paper compares two LEMFEV configurations: a propeller-based WT1 and a rocket engine-based WT3 fixed-wing aircraft. The use of the two power plant types produces aircraft different in shape and size, hence their aerodynamic and flight performance for the given payload mass [10].

The objective of this work is to quantitatively explore the differences between these LEMFEV configurations and establish suitable scientific missions. The study's findings will increase our knowledge of a Martian fixed-wing aircraft's payload mass capabilities as well as its planform geometry and suitable airfoils. The findings of this study will be applied to the design of other configurations of this science Martian UAV (mentioned in Table 1), with the final goal of selecting the most rational layout for a subsequent detailed design effort.

The remainder of this paper is organized as follows.

Section 2 briefly describes the MATLAB code developed for the LEMFEV design and analysis; justifies the selection of measures of merit for the project; and presents and justifies the most important mathematical models, system specifications, and estimated aerodynamic and stability performance of the aircraft. For aerodynamic predictions, XFLR5 was used. Section 3 reports and discusses the results of the trade studies, as well as the specifications for the WT1 and WT3 configurations. Sect. 4 draws conclusions from this study.

2 Methods: LEMFEV design and analysis

2.1 LEMFEV code structure

Figure 1 shows the structure of the MATLAB software developed for sizing and analysis of the WT1 and WT3 configurations. The main code is based on constraint analysis and unity equation. The unity equation iterations stop when an accuracy of 1% is reached. The main code takes data from the input block (solar irradiance, atmospheric parameters, baseline airfoil aerodynamic properties, design flight conditions, engine, systems, and equipment specifications). For calculating the solar radiation intensity on the Martian surface during the year, the "isotropic sky diffuse" model is used [11]. According to this model, the solar radiation intensity on a planet's surface is determined by three components: direct, scattered, and reflected radiation.

The data on solar radiation on Mars is largely based on geometric relationships between Mars and the Sun (solar radiation from the outer atmosphere). These data were refined to some extent based on the Mars atmospheric information collected during the operation of the Viking lander [11].

The function used in this work to estimate the duration of daylight hours on Mars is based on a mathematical model of Earth's daylight hours duration [12]. This model has been modified for Mars by replacing the expression for solar declination angle, which for Mars was taken from [11].

The code produces the aircraft and its component masses, as well as the wing area, required thrust, flight performance, rational airfoil and its aerodynamic properties, tail geometry, and a limited stability analysis for the relevant operating conditions. In this context, 'rational airfoil' means the airfoil that provides the greatest value of a measure of quality (discussed below) at the estimated design conditions.

In Fig. 1, W = weight [N]; E = endurance [min]; d = diameter [m]; S = wing area [m^2]; b= wing span [m]; AR = $\frac{b^2}{S}$ = wing aspect ratio [-]; T = thrust [N]; V_{cr} = cruise speed [m/s]; i = iteration number; P = power [W]; $V_{HT,VT}$ = horizontal and vertical tail volume coefficient [–]; $X_{AC,CG}$ = x-coordinate of aerodynamic center and center of gravity reduced by the length of mean aerodynamic chord (MAC) [–]; R = the ratio of solar cell area to wing area; m= mass [kg].

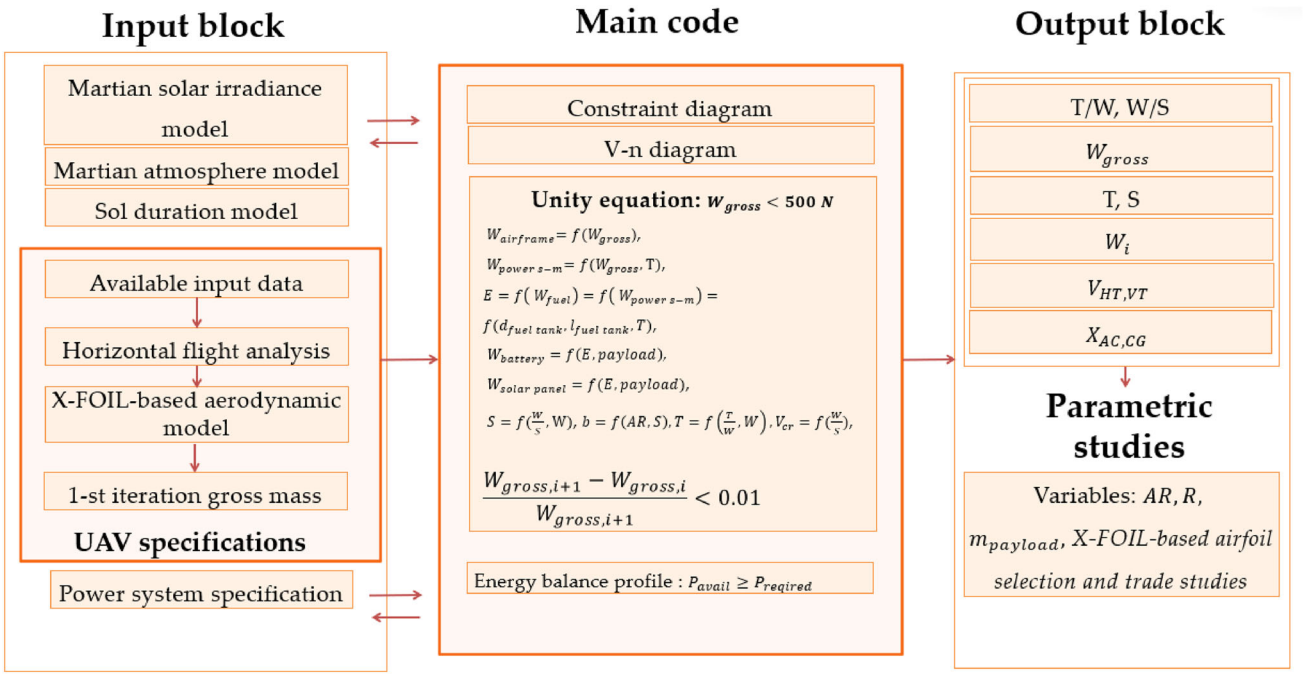

Fig. 1 The MATLAB code structure developed for the LEMFEV project

2.2 House of quality chart: selection of measures of merit for the LEMFEV

The house of quality chart shown in Fig. 2 was used to identify the measures of merit for the LEMFEV project.

The customer requirements, including reliability, payload mass, range, speed, and endurance, as well as the power available for instruments and the allowable mass of the data transmission system, were converted into aircraft parameters and properties. The analysis showed that in order to bring the maximum value to Mars exploration, the Martian airplane needs a power system that would feature the maximum possible operational time at the given payload mass. This will permit expansion of the range of measured parameters on a spatial and temporal scale. The operational time may be extended either by ensuring the overnight flight of a solar single-flight airplane or by providing a solar rechargeable airplane with a vertical take-off capability. Nevertheless, the LEMFEV versions using other types of power plants are also considered in this project for reference and comparison.

Among the customer requirements, the most important is the reliability and technical maturity of the UAV, which can be expressed, e.g., in terms of the mean operational hours before failure. At this early conceptual design stage, this requirement may be addressed by selecting systems and components with known and appropriate reliability characteristics.

2.3 Constraint diagram

The constraint diagram shown in Fig. 3 was used to establish the optimum wing loading W/S and thrust loading T/W for the WT1 and WT3 configurations.

In Fig. 3, V_{st} = stalling velocity; $C_{L,\max}$ = maximum lift coefficient.

The considered design cases included the following:

- T/W for a service ceiling (rate of climb at ceiling 0.508 m/s);
- T/W for a desired rate of climb;
- T/W for a desired cruise airspeed; and
- T/W for a level constant-velocity turn.

Also, the diagram shows what maximum lift coefficient the UAV's airfoil must have to satisfy the given stalling velocity and wing loading requirements. Higher wing loadings and lower stalling velocities call for exceedingly high maximum lift coefficients.

For reference, the diagram shows the design stalling velocity limit (which is the function of the UAV's weight and maximum lift coefficient), as well as the wing loading corresponding to the available load factor (maximum lift-to-weight ratio) for the given Mach number limitation (0.8).

The optimal design point permits establishing the wing and thrust loadings at which all the requirements are met. At the design stall limit of 52 m/s, the maximum allowable wing loading is approximately 25 N/m^2. The design thrust

Row #	Weight Chart	Relative Weight	Mars Science Importance (1-5)	Maximum Relationship	Customer Requirements (Explicit and Implicit) / Functional Requirements	Wing area	Power system type	Gross mass	Fuel mass	Fuselage midsection	Wing layout	Foldability	VTOL
					Column #	1	2	3	4	5	6	7	8
1	|||||||||||	24%	5	9	Reliable	▽	●	○	▽	▽	●	●	●
2	|||||||||	19%	4	9	Large payload	●	●	●	●	●	○	○	●
3	|||||||	14%	3	9	Long range	○	●	●	●	●	○	○	●
4	||||	10%	2	9	Low speed	●	●	●	▽	●	▽	○	●
5	|||||||	14%	3	9	Endurance	○	●	●	●	●	○	●	●
6	||||	10%	2	9	High power for instruments	●	○	●	●	●	▽	▽	○
7	||||	10%	2	9	Data transmission system	●	●	●	●	●	○	▽	○
					Technical Importance Rating	538	842	757	633	709	404	490	785
					Relative Weight	10%	16%	15%	12%	14%	8%	10%	15%

Fig. 2 The House of Quality Chart for prioritizing the measures of merit for the LEMFEV. Customer–Functional requirement relationships: ● Strong; ○ Moderate; ▽ Weak

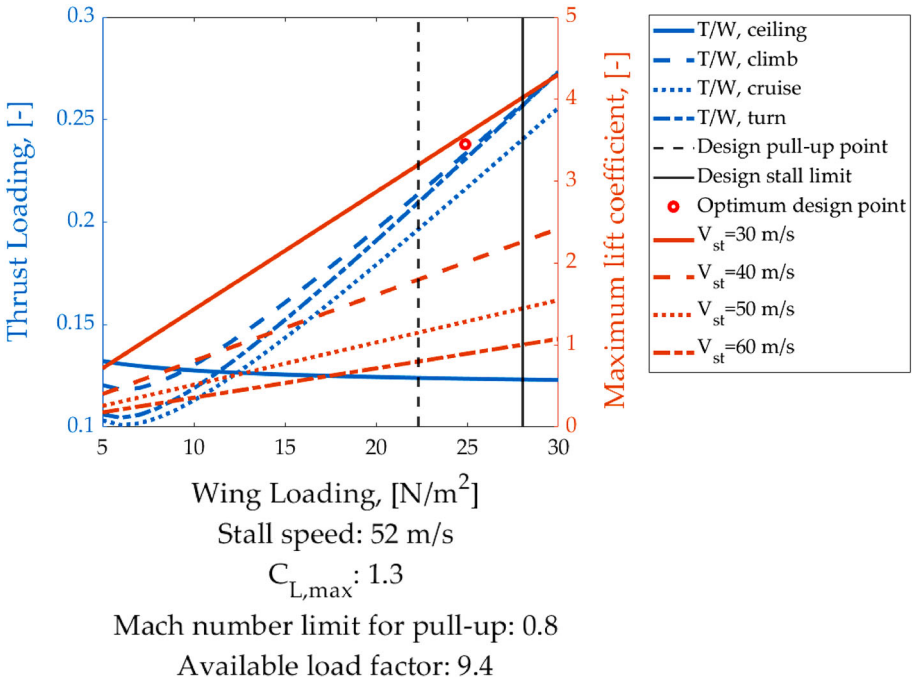

Fig. 3 WT1 and WT3 Constraint Diagram: AR 3, Payload 7 kg

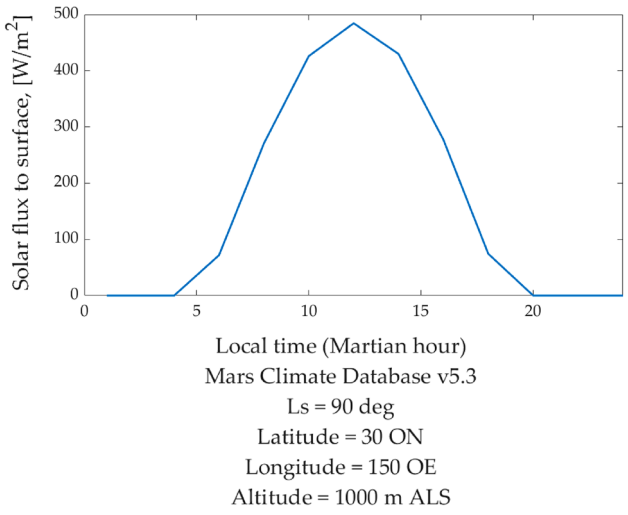

Fig. 4 Solar flux to surface with climatology average solar scenario [13]

loading is 0.24. The iterative solution of the unity equation yields the optimized value of the airplane's gross mass, hence the design wing area and thrust.

2.4 Irradiance model

The data on irradiance on Mars were obtained from the Mars Climate Database v5.3 [13] and are presented in Fig. 4. The irradiance depends on geographic location and time, weather conditions, and albedo [14]; in Fig. 4, an average solar scenario is shown.

In Fig. 4, L_s stands for aerocentric longitude [°].

2.5 Battery specifications

One of the key aspects of a solar UAV design is the selection of the battery and solar cells.

At present, a new type of sulfur cathode (Li–S) battery is being introduced into technical systems with high energy storage capacity demand. This technology begins to replace lithium-ion batteries.

The main advantages of Li–S over Li-ion batteries are the following:

- higher values of specific energy storage capacity, which for test samples may reach up to 500 Wh/kg [15];
- protection against overcharging is not required;
- wider operating temperature range; and
- safety in case of mechanical damage.

The main disadvantage is a large degradation due to charge–discharge cycles compared to Li-ion batteries. Also, this technology is still expensive for the commercial replacement of Li-ion batteries.

Table 2 WT1 and WT3 battery specifications

Parameter	Value	Description	Units
$E/m_{battery}$	500*3600	Battery specific energy	J/kg
$E/V_{battery}$	1000	Battery energy density	Wh/l
$\eta_{batterych/dch}$	0.97	Efficiency of charge/discharge process	–

Table 3 WT1 solar cell specifications

Parameter	Value	Description	Units
$\rho_{solarcell}$	0.49	Solar cell density	kg/m^2
$\eta_{solarcell}$	0.3	Solar cell efficiency	–

For preliminary estimations, Li–S batteries with a specific energy of 500 Wh/kg [16, 17] may be used, taking into account the mass of the battery case. The charge/discharge cycle efficiency is expected to reach 0.97 [18, 19]. The energy density is set to 1000 W•h/l [16, 17]. Table 2 shows the battery specifications used in the design of the WT1 and WT3 configurations.

2.6 Solar cells

A solar cell is a device that uses the photovoltaic effect to transform solar energy into electricity. It is very commonly employed in space applications because it enables a clean, long-lasting energy source that practically requires no maintenance.

Table 3 shows the solar cell specifications used in the design of the WT1 configuration. The data are based on [20].

2.7 WT1 energy balance

The energy balance profile compares the total energy required for flight, navigation, and scientific instruments to the energy available from the battery over a 24-h cycle. It accounts for the need to reduce the voltage for avionics and payload, the charge and discharge efficiency of the battery used for the overnight flight, and the efficiency of solar cells and the maximum power point tracker.

Figure 5 shows the energy balance profile for the WT1 configuration. The excess electrical power refers to the power available for charging the battery. Under estimated conditions, the UAV's battery can be charged during the day, so an overnight flight is possible.

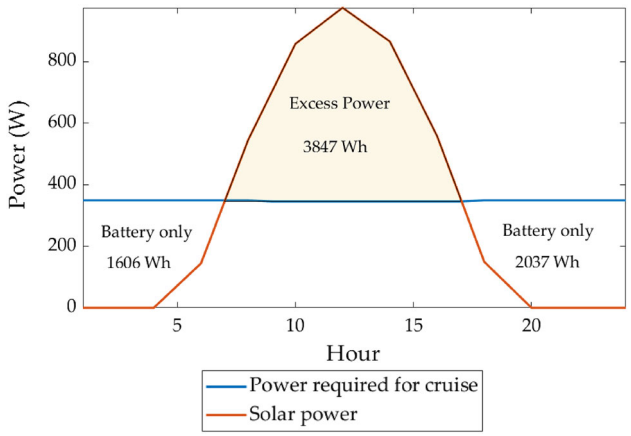

Fig. 5 WT1 configuration. Cruise energy balance profile: AR 3, altitude 1000 m, Re 1.18e + 05, C_l 0.85

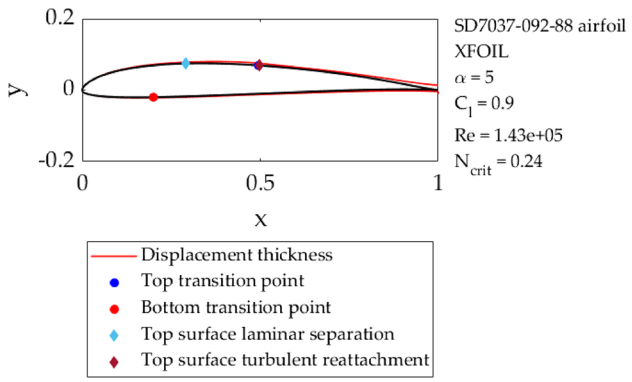

Fig. 6 The SD7037 092 88 airfoil

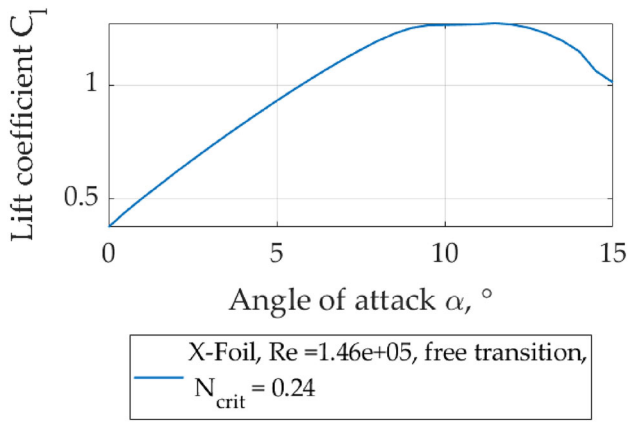

Fig. 7 The SD7037 092 88 airfoil, lift curve

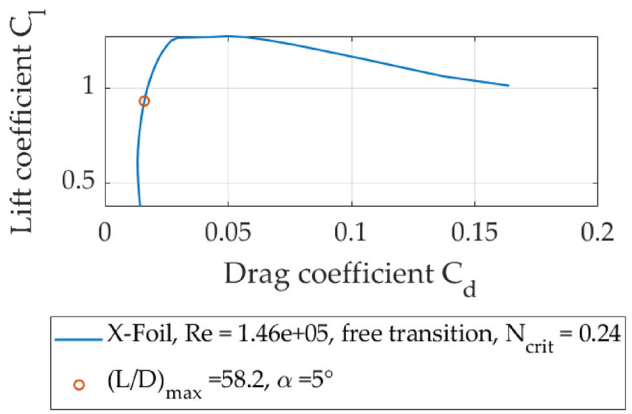

Fig. 8 The SD7037 092 88 airfoil, drag polar

2.8 LEMFEV airfoil properties

As a result of the optimization procedure, for the estimated design conditions, the SD7037 092 88 airfoil was selected.

For airfoil aerodynamic analysis, the XFLR5 software [21] was used. It applies a linear-vorticity second-order accurate panel method for inviscid analysis and couples it with an integral boundary layer method and an e^N- type transition amplification formulation using a global Newton method to compute the inviscid/viscous interaction. It also includes a compressibility correction as well as tuned correlations for turbulence and transition that extend its applicability, and is especially important for modeling the Martian atmosphere with a low density and a low speed of sound. One of the limitations of XFLR5 is that it assumes an instantaneous transition to turbulent flow when the trip location is specified on the airfoil surface. The accuracy of the XFLR5 predictions has been thoroughly analyzed (for example, [22–24]) and is considered reasonable within the limitations of the numerical and physical models it is based on, and provided that the simulation results are interpreted correctly. The simultaneous solution of the boundary layer and inviscid equations by a global Newton method makes XFLR5 adequate for treating airfoils which tend to produce laminar bubbles. In [24], the computed polar for the Eppler 378 airfoil at three low Reynolds numbers (200 000, 100 000, and 60 000) was compared to the measurements reported in [25]. The overall agreement seems satisfactory, with the accuracy sufficient for the scope of the current study.

The SD7037 092 88 airfoil, as well as the locations of transition, separation, and reattachment points under the design conditions, is shown in Fig. 6.

The amplification factor $N_{\text{crit}} = 0.24$ was used to model the 20% turbulence intensity of the Martian atmosphere.

The lift curve, drag polar, transition point, and laminar bubble size as functions of angle of attack, as well as the pressure, skin friction, and velocity chordwise distributions for the SD7037 092 88 airfoil at the cruise conditions, are shown in Figs. 7, 8, 9, 10, 11, and 12, respectively.

The XFLR5 simulation showed that the SD7037-092-88 airfoil under the given conditions features a mild stall at the angle of attack $\alpha_{\text{crit}} \approx 9°$ (Fig. 7), the maximum lift-to-drag ratio $(L/D)_{\max} \approx 58$ at $\alpha = 5°$ (Fig. 8), and a smooth

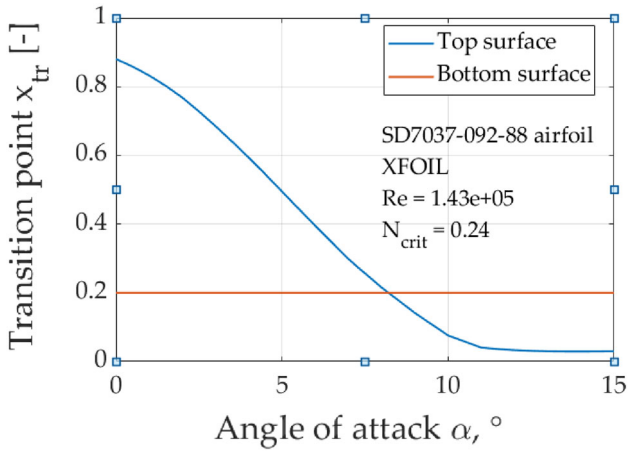

Fig. 9 The SD7037 092 88 airfoil, transition point as a function of angle of attack

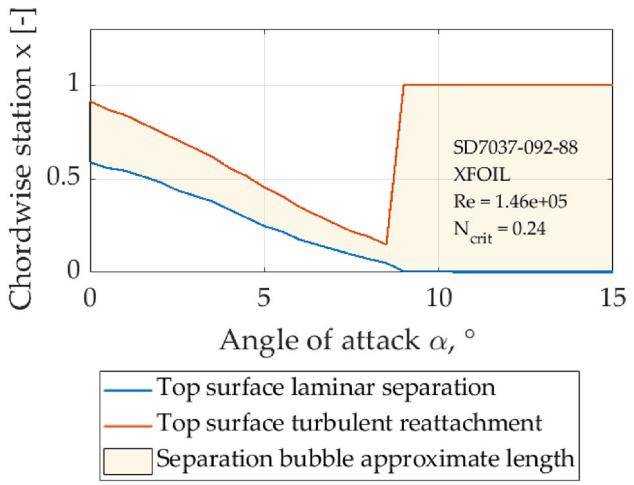

Fig. 10 The SD7037 092 88 airfoil, laminar bubble size as a function of angle of attack

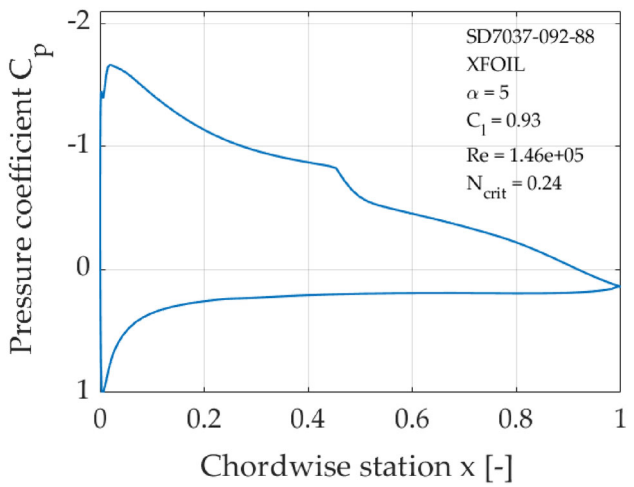

Fig. 11 The SD7037 092 88 airfoil, pressure coefficient

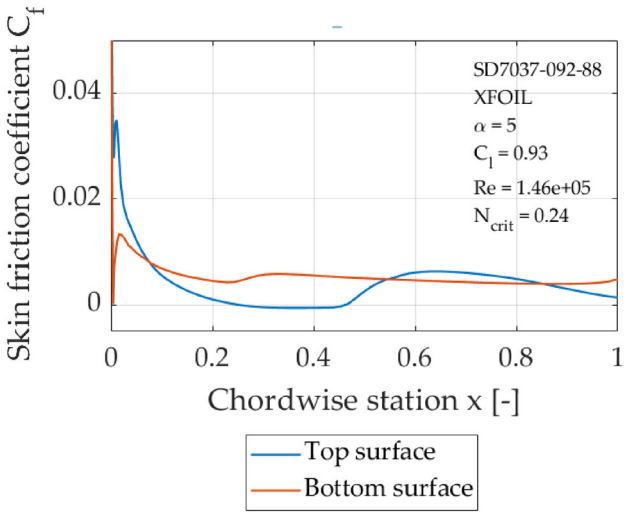

Fig. 12 The SD7037 092 88 airfoil, skin friction coefficient

movement of the transition point upstream with an increasing angle of attack (Fig. 9). This airfoil forms a laminar bubble over the entire range of angles of attack (Fig. 10); nevertheless, a portion of the lift curve can still be modeled linear up to an angle of attack of 6 or 7°. At the design angle of attack of 5°, the length of the laminar bubble is approximately 25% of the chord length (Figs. 10, 12), and the bubble thickness, as far as it can be judged from the pressure distribution, is relatively thin (Fig. 11). The smaller the bubble thickness, the lower the pressure drag increase at a given increase in lift, and the less likely it is that transition trips can improve the airfoil performance [26].

Some aerodynamic characteristics of the SD7037 092 88 airfoil are shown in Table 4. In Table 4, $C_l|L/D_{\max}$ denotes the lift coefficient corresponding to the maximum lift-to-drag ratio; $\Delta C_l = C_{l,\max} - C_l|L/D_{\max}$.

2.9 LEMFEV tail design and longitudinal stability analysis

The WT1 and WT3 configurations feature a conventional aft tail with all-movable horizontal and vertical stabilizers. The reason for using all-movable horizontal and vertical tails is the reduction of the wetted area and drag for the given stability margin and control authority. The conventional tail configuration was selected for the single-flight Martian airplane as it typically provides the required characteristics at a low structural weight.

Since the LEMFEV features an extremely low aspect ratio wing (3), rather than using a historical value of the HT volume coefficient, it was estimated and set such that the design center of gravity envelope could be achieved by the aircraft.

For both horizontal and vertical tails, the NACA 0008.2 airfoil was selected.

Table 4 Some aerodynamic characteristics of the SD7037 092 88 airfoil

Airfoil	L/D_{max}	$C_l \vert L/D_{\max}$	$C_{l,\max}$	ΔC_l
SD7037-092–88 airfoil	71.9	0.95	1.30	0.35

The required horizontal tail volume coefficient, among others, depends on the design longitudinal stability margin.

For some reduction in trim penalties, a wing-tail UAV may be designed to be statically unstable. In this case, to balance the UAV, the control surface produces positive lift; therefore, the lift demands on the wing are reduced:

$$C_{L,\,\text{trim, unstable}} = \left[1 + \frac{\bar{x}_{CG} - \bar{x}_{AC}}{\bar{x}_{HT,\,AC} - \bar{x}_{CG}}\right], \tag{1}$$

where

$C_{L,\,\text{trim, unstable}}$ = the trimmed aircraft lift coefficient;

$\bar{x}_{CG}$ = the aircraft center of gravity location reduced by the chord length;

$\bar{x}_{AC}$ = the untrimmed aircraft aerodynamic center location reduced by the chord length;

$\bar{x}_{HT,\,AC}$ = the horizontal tail aerodynamic center location reduced by the chord length.

However, there are limits to the degree of instability that can be introduced into an aircraft configuration while maintaining control authority, since control authority diminishes with increasing instability [27]. Therefore, the benefit of static instability comes from the increased lift-to-drag ratio at a steady state trimmed condition rather than in terms of maneuverability. In practice, the instability level may be restricted due to the limitations associated with the available control surface effectiveness, control surface rates, or limited achievable stability margins. Also, it was shown the following:

- the maximum control authority with a given control system corresponds to a neutrally stable configuration. The control authority is lower for more unstable as well as more stable configurations;
- for an unstable aircraft, the achievable nose-down pitching moment at high angles of attack is limited by the amount left when trimming deflections are subtracted;
- even though more unstable airplanes are less affected by vertical wind gusts, the control surface deflection needed to counteract a certain disturbance is greater than that of a stable aircraft due to a decreased control authority.
- an unstable aircraft can be made artificially stable, but only within a region where the available control authority is sufficient.

Figure 13 allows selecting the horizontal tail volume coefficient V_{HT} for the WT3 and WT1 configuration with a static instability of 5% of the mean aerodynamic chord (MAC) and the stabilizer incidence angle of 5°. The narrower the design center of gravity envelope, the smaller the required horizontal tail volume coefficient.

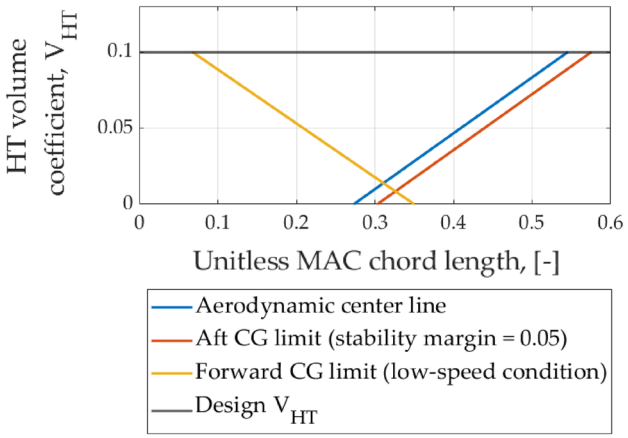

Fig. 13 WT1 and WT3 configurations. Available center of gravity envelope as a function of the horizontal tail volume coefficient

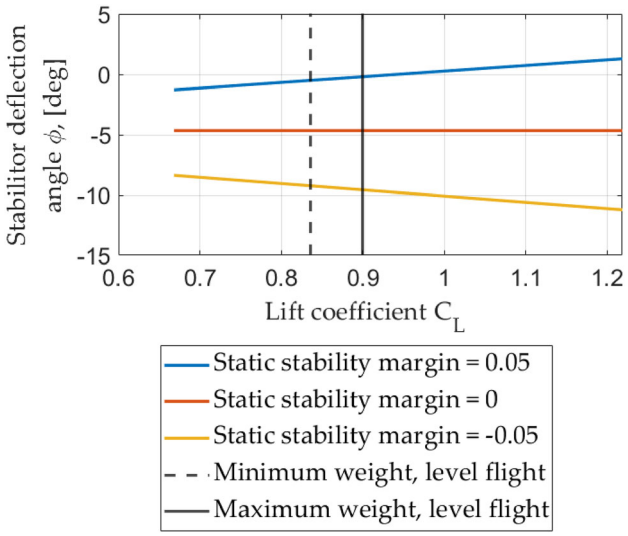

Fig. 14 WT1 and WT3 configurations. Trim curves at various stability margins

The aft center of gravity limit is defined by the airplane's aerodynamic center and the design instability margin; the forward center of gravity limit is set by the requirement to trim the aircraft at stalling speed with the maximum deflection of the stabilizer.

Figure 14 shows the UAV's trim curves at various stability margins.

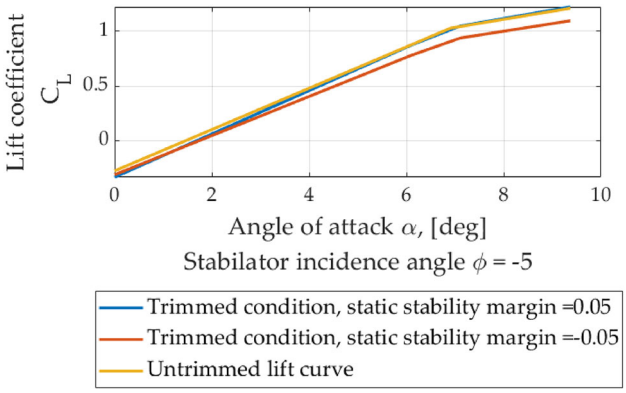

Fig. 15 WT1 and WT3 configurations. Baseline and trimmed lift curves

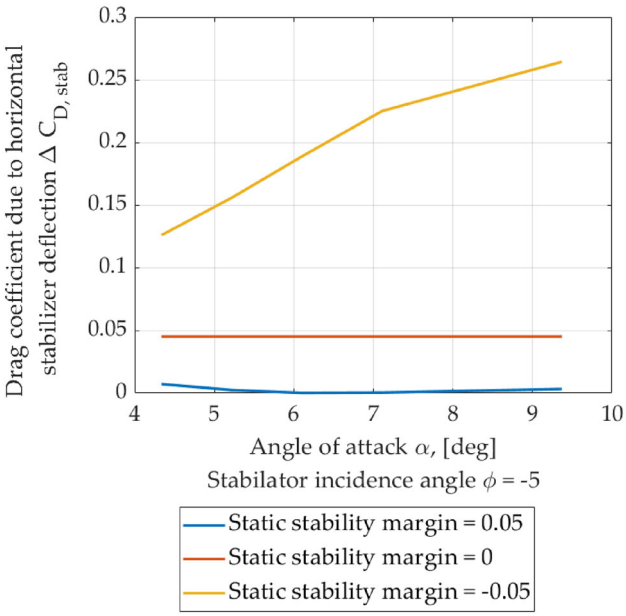

Fig. 16 WT1 and WT3 configurations. Drag coefficient due to elevator deflection at various stability margins

The required stabilizer deflection angle φ at the trimmed cruise condition is close to $-5°$ for the statically neutral case and approaches zero for the 5% instability case. Taking into account the extremely low Reynolds numbers expected for the stabilizer (around $4e+04$), the stabilizer deflection angle φ was limited to $\pm 10°$. It is evident from Fig. 14 that, with this limitation, a stable aircraft cannot be trimmed at lift coefficients exceeding 0.95.

As expected, static stability comes with some trim penalties in terms of lift slope (Fig. 15) and drag coefficient (Fig. 16). The data in Figs. 15 and 16 were obtained by converting the 2-D XFLR5 predictions to the UAV's evaluated geometry.

With the stabilizer set to 5°, the pitching moment coefficient of a statically neutral aircraft is brought to zero (Fig. 14). However, the least trim drag penalties are associated with the unstable configuration (Fig. 16).

3 Results and discussion: LEMFEV specifications

In order to explore the design space available for the WT1 and WT2 configurations and compare them, a series of trade studies were conducted. The problem setting was as follows.

Variables:

- wing aspect ratio $AR = 2, 3, 6$;
- payload mass $m_{payload} = 5, 10, 15\ kg$;
- fuel tank length $l_{fueltank} = 0.4 \ldots 1.6m$with$0.2m$step; and
- solar cell area ratio $R_{solarcell} = 0.8 \ldots 1.6$with$0.2$step.

Functions:

- airplane gross mass m [kg];
- wing span b [m];
- engine runtime T [min];
- excess solar power P_{excess} $[W]$; and
- cruise speed [m/s].

For the WT1 configuration, the operating region on Mars was set as follows:

- latitude 30°;
- longitude 150°;
- altitude $1000m$; and
- aerocentric longitude 90°.

The results of the trade studies are shown in Figs. 17, 18.

Within the adopted design space, the WT3 engine operating time (which is a function of the fuel tank length) varies between 6 and 17 min, with the gross mass being 45–105 kg (Fig. 17) and the wing span being 4.5–6.7 m (Fig. 19). In the selected operating region, the WT1 configuration is optimized to be capable of a continued day-night flight; its gross mass is 34—65 kg (Fig. 20), and its wing span varies from 3.9 to 5.4 m (Fig. 18). As expected, the wing aspect ratio significantly affects the airplane gross mass (Figs. 21, 22).

Figures 23 and 24 show the mass breakdown for the two configurations at the same values of wing aspect ratio and payload mass as a function of the aircraft wing span. The power plant mass is the greatest mass contribution to the WT3 configuration, despite the extremely low wing loading of 25.6 N/m^2 (see Table 5) and a relatively high airframe mass ratio.

Figure 25 shows the comparison of the two configurations in terms of mass ratios. Payload mass ratio, as follows from

Table 5 WT1 and WT3 specifications

Parameter	WT1	WT3	Description	Units
Flight conditions				
H	1000	1000	Altitude	m
Lat	30	–	Latitude	degrees
Lon	150	–	Longitude	degrees
L_t	90	–	Aerocentric longitude	degrees
Weight/mass specification				
M	40	64	Aircraft gross mass	kg
W	147	237	Aircraft gross weight	N
m_{payload}	7	7	Payload mass	kg
m_{airframe}	16	25	Airframe mass	kg
m_{fuel}	–	19	Fuel mass	kg
$m_{\text{solarcell}}$	3	–	Solar cell mass	kg
m_{battery}	8	0.1	Battery mass	kg
Aircraft geometric characteristics				
S	5.9	9.3	Wing area	m^2
b	4.2	5.3	Wing span	m
c_{MAC}	1.46	1.85	Wing mean aerodynamic chord	m
l_{fueltank}	–	0.8	Fuel tank length	m
d_{fueltank}	–	0.2	Fuel tank diameter	m
General aircraft characteristics				
T	35	56	Thrust	N
E	–	12	Endurance	min
R	–	46	Range	km
V_{cr}	65	64	Cruise speed	m/s
V_{min}	52	52	Minimum speed	m/s
Non-dimensional parameters				
m/S	6.7	6.8	Wing loading	kg/m^2
W/S	25	25	Wing loading	N/m^2
T/W	0.24	0.24	Thrust loading	–
AR	3	3	Aspect ratio	–
λ	0.5	0.5	Taper ratio	–
Operating conditions				
Re	1.18e + 05	1.46e + 05	Reynolds number	–
M	0.28	0.3	Mach number	–
$C_{l,\text{cruise}}$	0.85	0.9	Cruise lift coefficient	–
Wing airfoil: SD7037 092 88				
Tail airfoil: NACA 0008.5				

the House of Quality Chart, Fig. 2, is one of the measures of merit for the project. Other important parameters are the airframe mass ratio and the power system mass ratio. The power system includes the components required to produce energy for flight. For WT1, these are the motor, maximum power point tracker, gearbox, controller, propeller, solar cells, and battery. For WT3, these are the rocket engine, hydraulic system, fuel tank, high-pressure vessel with helium, and fuel. The ratios are shown as a function of wing span, since the wing span limits the foldability of the Martian airplane.

It follows from Fig. 25 that the electric WT1 configuration outperforms the rocket-based WT3 configuration on all selected parameters.

In Table 5, the WT1 and WT3 specifications are given. These include the flight and design conditions, weight specification, aircraft geometric and performance characteristics for a payload mass of 7 kg, and a wing aspect ratio of 3.

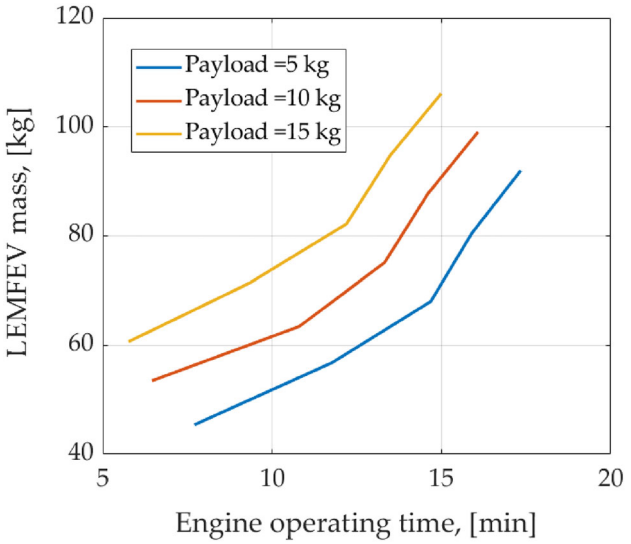

Fig. 17 WT3, AR 3, Gross mass—engine runtime, alt 1000 m, Re 1.48e + 05, C_l 0.9

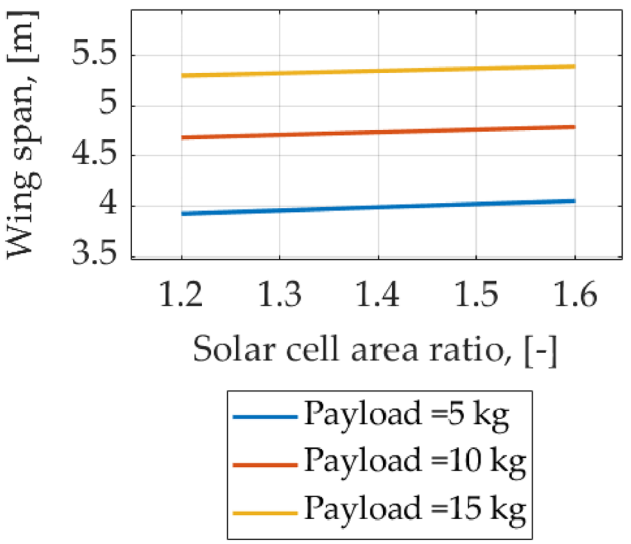

Fig. 18 WT1, AR 3, Wing span—solar cell area ratio, alt 1000 m, Re 1.2e + 05, C_l 0.85

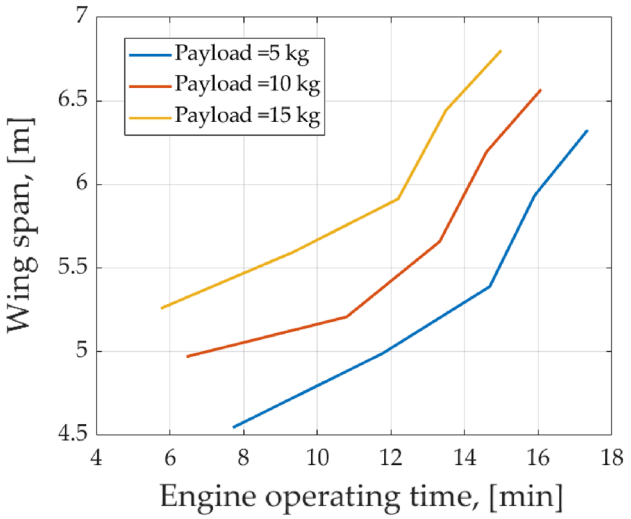

Fig. 19 WT3, AR 3, Wing span—engine runtime, alt 1000 m, Re 1.48e + 05, C_l 0.9

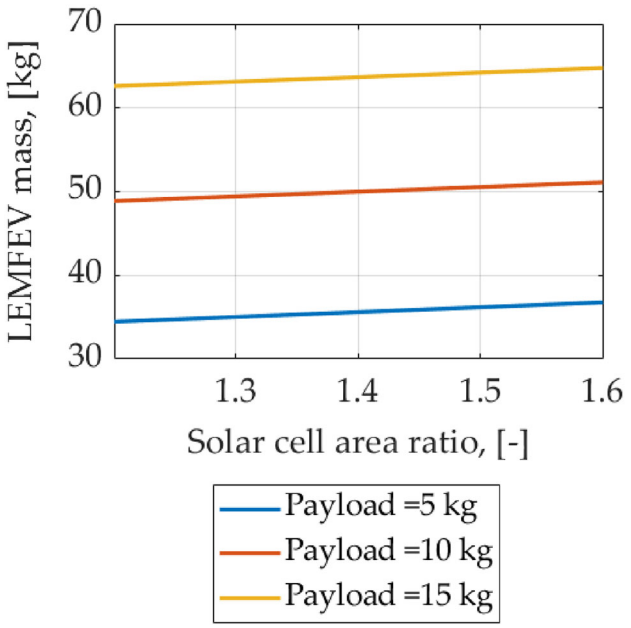

Fig. 20 WT1, AR 3, Gross mass—solar cell area ratio, alt 1000 m, Re 1.2e + 05, C_l 0.85

The comparison of geometries of the WT1 and WT3 configurations is shown in Fig. 26 (top view) and Fig. 27 (side view). Figures 28 and 29 show the WT3 and WT1 configurations folded and mounted in an aeroshell.

The optimized versions of the two configurations feature the same wing and tail airfoils, the same wing and tail planforms, and different dimensions and weights. The two aircraft have similar cruise speeds and are designed to carry the same payload. The need to place the rocket engine, fuel tank, and pressurized vessel in the fuselage renders the WT3 configuration more challenging to size.

The theoretical day–night flight of a solar Martian airplane became possible due to advancements in battery technology. With the battery specific energy being lower than 400 Wh/kg, at Martian solar irradiation, the battery cannot be charged during the daytime to ensure an overnight flight.

4 Conclusions

In this study, a rocket-based UAV and a solar wing-tail Martian UAV were designed and assessed against a set of criteria

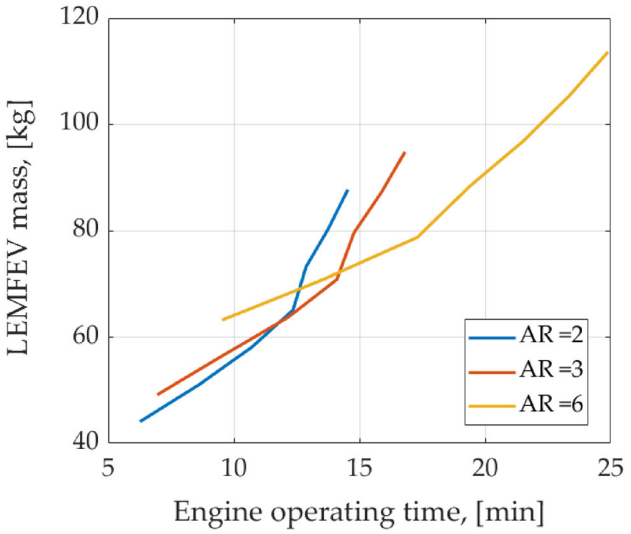

Fig. 21 WT3, Payload 7 kg, Gross mass—engine runtime, alt 1000 m, Re 1.48e + 05, C_l 0.9

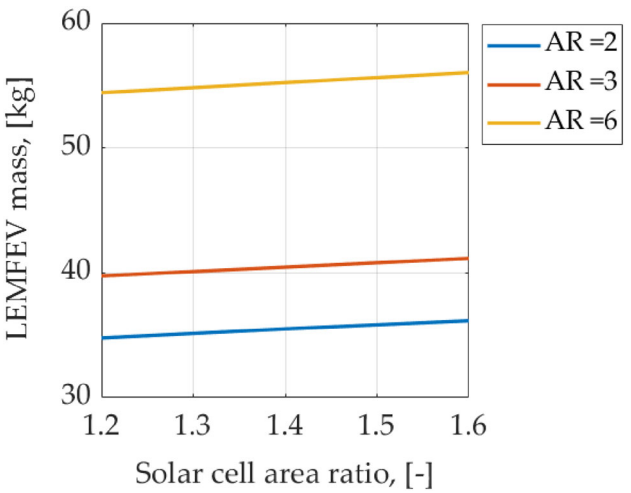

Fig. 22 WT1, Payload 7 kg, Gross mass—Solar cell area ratio, alt 1000 m, Re 1.2e + 05, C_l 0.85

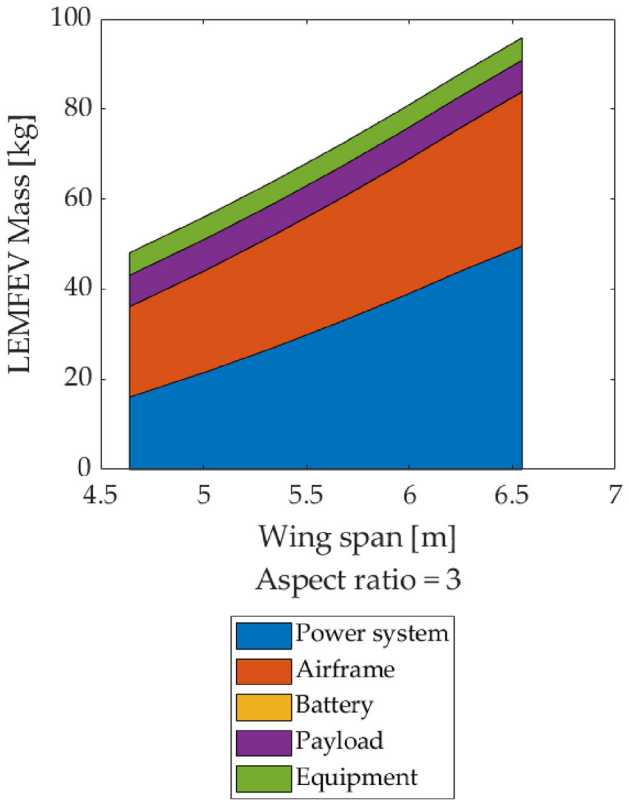

Fig. 23 WT3 Mass breakdown, payload 7 kg, AR 3

established using a house of quality chart. For the design and analysis, MATLAB and XFLR5 were used.

The uncertainty of the predicted results is related to the limited accuracy of the input data (e.g., system specifications and Martian atmospheric conditions) as well as the empirical mathematical formulations used in XFLR5.

The endurance of the rocket-based aircraft is limited by the fuel tank volume and fuel mass; however, the operating area of this aircraft is not restricted to the regions, seasons, and days with high solar irradiance. Therefore, for example, it can explore the depths of craters and canyons and, if a single soft landing option is possible, it can also serve as a stationary platform. Theoretically, the endurance of the solar UAV is unlimited; the drawback is that it can only operate under specific atmospheric conditions. Since the solar irradiance depends on the geographic location, aerocentric longitude, and albedo, the success of the mission performed by a solar UAV is highly uncertain. A suitable scientific mission for a solar single-flight UAV may be the measurement of atmospheric parameters to obtain turbulent and radiative fluxes over the lowest 2–10 km of the atmosphere. This will allow us to expand the geographical and temporal coverage of measurements currently available for the planetary boundary layer of Mars.

The results of the study extend our understanding of the capabilities of a Martian fixed-wing airplane in terms of payload mass hence its scientific value, as well as in terms of its planform geometry and airfoil shapes.

The findings of this study will be applied to the design of other configurations of this science Martian UAV, with the final goal of selecting the most rational layout for a subsequent detailed design effort.

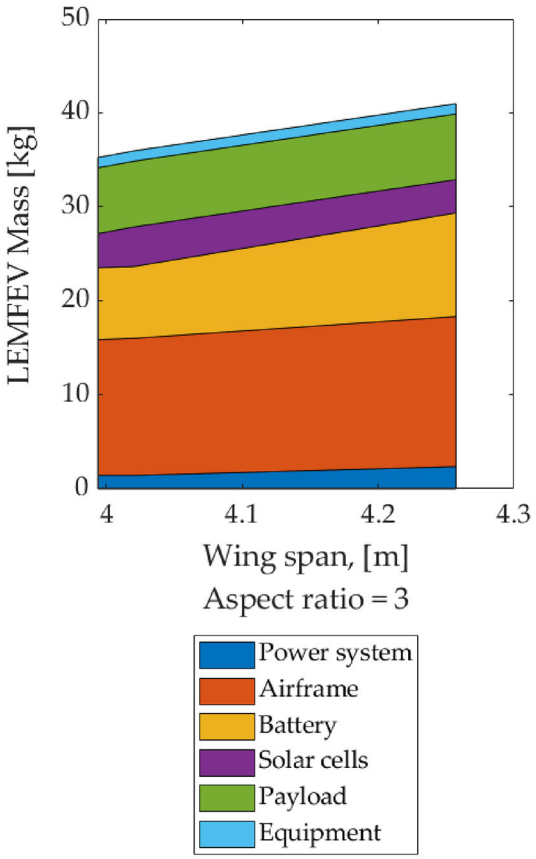

Fig. 24 WT1 Mass breakdown, payload 7 kg, AR 3

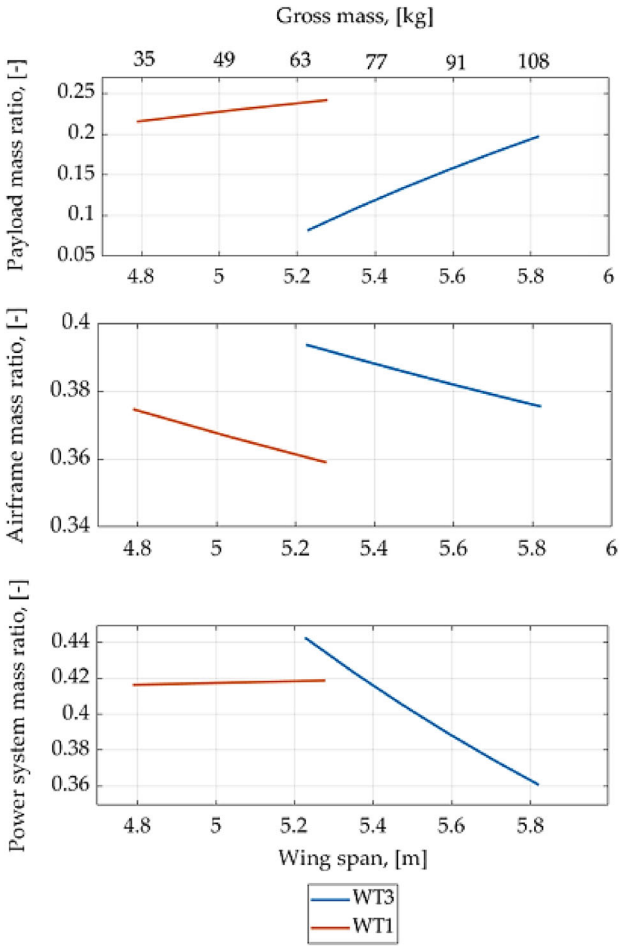

Fig. 25 WT1-WT3 mass ratios. WT3: AR 3, fuel tank length 0.8 m, C_l 0.9. WT1: AR 3, solar cell area ratio 1.1, C_l 0.85

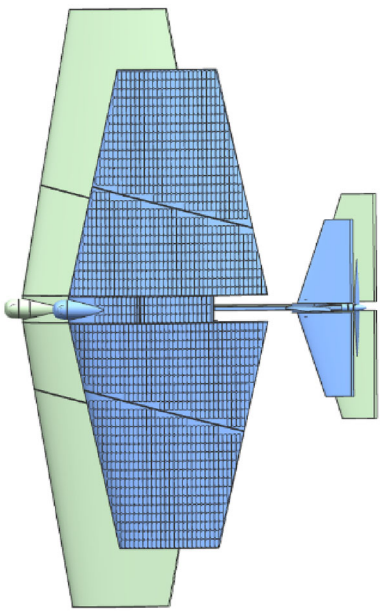

Fig. 26 WT1 vs WT3 configurations. Top view

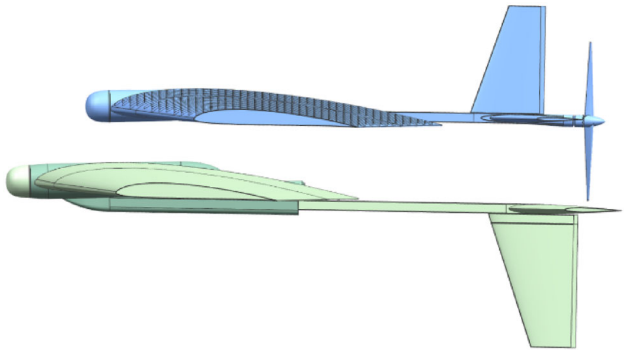

Fig. 27 WT1 vs WT3 configurations. Side view

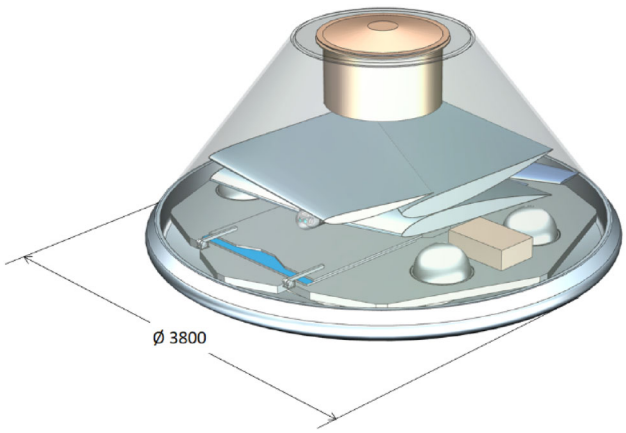

Fig. 28 Folded WT3 configuration inside an aeroshell

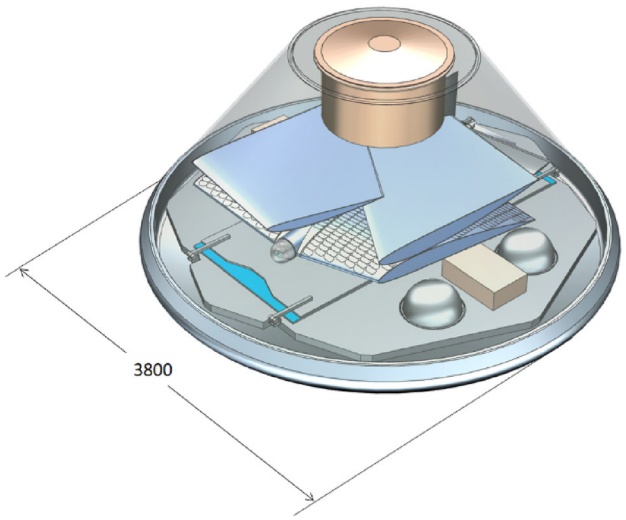

Fig. 29 Folded WT1 configuration inside an aeroshell

Funding This research was funded by the Russian Science Foundation, grant number 22–49-02047.

Data availability All research data are available upon request.

Declarations

Conflict of interest The authors have no relevant financial or non-financial interests to disclose.

References

1. Reed RD (1978) High-flying mini-sniffer
2. Gasbarre JF, Dillman RA (2003) Preliminary design and analysis of the ARES atmospheric flight vehicle thermal control system
3. NASA (2013) A concept study of a remotely piloted vehicle for mars exploration, NASA
4. Kearns J, Usui M, Smith SW, Scarborough SE, Smith T, Cadogan DP (2004) Development of UV-curable inflatable wings for low-density flight applications
5. Jacob JD, Lumpp JE, Smith SW, Smith WT (2006) Multidisciplinary design experience of a high altitude inflatable wing UAV for aerospace work force development
6. Benito J et al (2017) Hybrid propulsion mars ascent vehicle concept flight performance analysis. In: IEEE Aerospace Conference
7. Bar-Cohen Y, Colozza A, Badescu M, Sherrit S, Bao X (2012) biomimetic flying swarm of entomopters for mars extreme terrain science investigations
8. Colozza A, Miller C, Reed B, Kohout L, Loyselle P (2001) Overview of propulsion systems for a mars aircraft
9. Hanbing S, Underwood C (2007) A Mars VTOL Aerobot - preliminary design, dynamics and control. In: IEEE Aerospace Conference Proceedings, Guildford
10. Liu L, Cao X, Zhang X, He Y (2020) Review of development of light and small scale solar/hydrogen powered unmanned aerial vehicles. Acta Aeronaut Astronaut Sin 41(3):623
11. Appelbaum J, Landis GA, Sherman IR (1990) Solar radiation on Mars. Update 1991. Sol Energy 50:35–51
12. Forsythe WC, Rykiel EJ, Stahl RS, Wu H, Schoolfield RM (1995) A model comparison for daylength as a function of latitude and day of year. Ecol Model 80:87–95
13. Mars Climate Database v5.3 (2023) [Online]. Available: http://www-alternate-mars.lmd.jussieu.fr/mcd_python/
14. Noth A (2008) Design of solar powered airplanes for continuous flight. Url: [PDF] Design of solar powered airplanes for continuous flight. Semantic Scholar
15. INSIDEEVs (2023) [Online]. Available: https://insideevs.com/news/394309/oxis-cells-almost-500-wh-kg/
16. Ionel S (2023) High Energy Density Lithium Ion Cells with Silicon Nanowire Anode Technology, 26 08 2023. [Online]. Available: https://www1.grc.nasa.gov/wp-content/uploads/5.-Amprius.pdf
17. Dörfler S et al (2021) Recent progress and emerging application areas for lithium–sulfur battery technology. Energy Technol 9(1):2000694
18. Вестник НПО имени С.А. Лавочкина, №4, Москва, 2017, p 122
19. Mikhaylik YV, Kovalev I, Schock R, Kumaresan K, Xu J, Affinito J (2010) High energy rechargeable Li-S cells for EV application: status, remaining problems and solutions. ECS Trans 25(35):23–34
20. Rocket lab. [Online]. Available: https://www.rocketlabusa.com/space-systems/solar/space-solar-cellscics/. Accessed 27 Aug 2023

21. Drela M. "XFOIL". Available: https://web.mit.edu/drela/Public/web/xfoil/
22. Deperrois A. Available: http://www.xflr5.tech/docs/Results_vs_Prediction.pdf
23. Coder J, Maughmer M (2014) Comparisons of theoretical methods for predicting airfoil aerodynamic characteristics. J Aircr 51(1):183–191
24. Drela M (1989) XFOIL: an analysis and design system for low Reynolds numbers airfoils. Low Reynolds Number Aerodynamics, https://web.mit.edu/drela/Public/papers/xfoil_sv.pdf
25. Mcghee R, Jones G, Jouty R (1988) Performance characteristics from wind-tunnel tests of a low-Reynolds-number airfoil. AIAA, vol. 88, no. 6070
26. Lyon CA, Selig VS, Broeren AP (1997) Boundary layer trips on airfoils at low Reynolds numbers. In: 35th Aerospace Sciences Meeting & Exhibit, llinois
27. Johansson E (2018) Implications of designing unstable aircraft from a flight control perspective," http://www.diva-portal.org/smash/get/diva2:1380845/FULLTEXT01.pdf